RESEARCH ARTICLE

NANO · MICRO small
www.small-journal.com

In Situ Intrinsic Self-Healing of Low Toxic Cs_2ZnX_4 (X = Cl, Br) Metal Halide Nanoparticles

*Ben Aizenshtein and Lioz Etgar**

This study reports on the intrinsic and fast self-healing ability of all inorganic, low-toxic Cs_2ZnX_4 (X = Cl, Br) metal halide nanoparticles (NPs) when subjected to local heating by electron beam irradiation in high-resolution transmission electron microscopy (HR-TEM). The local heating induces the creation of nanoshells (NSs) following the template of the corresponding NPs, which are subsequently healed back to their original state within several minutes. Energy dispersive spectroscopy (EDS) and fast Fourier transform (FFT) analysis reveal that the composition, phase, and crystallographic structure of the original NPs are restored during the self-healing process, with a thin crystalline layer observed at the bottom of the NSs acting as the healing template. The inelastic scattering of the electron beam energy generates local heat that causes rapid atomic displacement, resulting in atomic mobility that lowers the density of the material and leads to NS formation. A unique insitu TEM heating stage measurement demonstrates the appearance of identical damage and self-healing to those induced by the electron beam. The NPs exhibit excellent stability under ambient conditions for up to a month, making them suitable for self-healing scintillators and other optoelectronic applications that require atomic-scale stability and healing.

1. Introduction

In recent years, there has been a surge of interest in materials possessing self-healing properties due to their potential to enhance the functionality of a wide range of applications that require stability and healing over prolonged periods. However, the majority of reports on such materials have discussed systems involving external additions and stimuli to initiate the healing process following the creation of damage. These external agents activate self-healing mechanisms that aid in restoring the mechanical, chemical, or physical properties of the damaged material.

A variety of self-healing systems have been reported in the literature, including those based on different mechanisms of polymers,[1,2] such as cross-linking, hydrolysis, and condensation, as well as sol–gel coating systems and organic and inorganic networks.[3] Cycloaddition[4] is another common self-healing system, and heterogeneous systems[5] of separate phases have been investigated, such as a liquid that fills fractures and solidifies. Additionally, host–guest-based preventive systems,[1] such as cyclodextrin, have been explored, which can bind to hydrophobic factors at the edges of damaged areas to prevent further damage.

However, the self-healing mechanisms discussed above are primarily achieved through the addition of complex external agents, mainly consisting of polymers. Such healing ability is not an intrinsic property of the material. Furthermore, these systems typically require external stimuli to initiate the healing process, such as light, pH, temperature, and pressure. Additionally, these external agent-based healing mechanisms are predominantly suitable for macro healing and macro damage and are generally not capable of dealing with the healing of micro or nano-damages, such as defects at the atomic scale. Moreover, the healing scale time of the above-mentioned systems is usually ranging between hours to days. Reports on intrinsic spontaneous fundamental self-healing of nanosystems and especially semiconductors are relatively rare. [6] Among them, the healing of nanoscale damage in $MPbBr_3$ has been reported[7] and the intrinsic self-healing of voids created in $Cs_2AgInCl_6$ double perovskite nanoparticles.[8]

Cs_2ZnX_4 is a well-known metal-halide material, which has promising properties for use as a scintillator,[9] enabling the detection of incoming ionizing electromagnetic energy through its conversion to ultraviolet (UV) and visible (vis) light. Cs_2ZnX_4 is characterized by a fast auger-free luminescence component[10,11] due to its wide band gap.[12] This material has an orthorhombic symmetry[12] and is iso-structural with β-K_2SO_4 and Cs_2CuCl_4, with $M(ii)X_4^{-2}$ units in tetrahedral geometry occupying the unit cell. Doping Cs_2ZnCl_4 with Co^{+2}, Te^{+4},[12] and Sb^{+3} [13–15] provides an emission at the infrared,[16] which improves the scintillator properties. Recently, Cs_2ZnX_4 has been investigated for its

B. Aizenshtein, L. Etgar
Institute of Chemistry
The Center for Nanoscience and Nanotechnology
Casali Center for Applied Chemistry
The Hebrew University of Jerusalem
Jerusalem 91904, Israel
E-mail: lioz.etgar@mail.huji.ac.il

The ORCID identification number(s) for the author(s) of this article can be found under https://doi.org/10.1002/smll.202305755

DOI: 10.1002/smll.202305755

potential use as a semiconductor in optoelectronic applications such as light emitting diodes (LEDs),[13,17] driven by the demand for non-toxic elements for use in these applications. Several reports[17,18] have been published to date on the synthesis and structure of Cs_2ZnX_4 nanoparticles.

In this study, we reveal and study the intrinsic self-healing abilities of Cs_2ZnX_4 (X = Cl, Br) nanoparticles at the atomic level under electron beam energy irradiation. Our results demonstrate that the self-healing capabilities of Cs_2ZnX_4 can be classified into three types: i) dynamic self-healing, ii) the creation of nano-shells by the e-beam and subsequent self-healing back to their original full nano-particle form, and iii) full healing without leaving any residual damage. Using fast Fourier transform (FFT) and Energy dispersive spectroscopy (EDS) analyses, we confirm that the original crystallographic characteristics, composition, and quantity of the material remain intact after the various self-healing processes. Moreover, the study was extended to various irradiation conditions, in order to investigate the relationship between the size of damage caused and the applied dose and acceleration voltage. In situ TEM heating stage measurements reveal that the damage and healing processes can result from direct heating, which are similar to those observed with electron beam irradiation. These lead-free and low-toxicity nanoparticles demonstrate structural and optical stability for over a month of measurements, making them suitable for direct use as scintillators with self-healing capabilities, as well as for other optoelectronic applications that require atomic-level stability and healing capabilities over time.

2. Results

The Cs_2ZnX_4 (X = Cl, Br) nanoparticles (NPs) have been found to exhibit two main phases: an orthorhombic[12] crystal structure with Pnam space group and a tetragonal crystal structure having the composition Cs_3ZnX_5. In this study, Cs_2ZnX_4 NPs were synthesized in which the unit cell is occupied by tetrahedrons of zinc connected to four halides, with cesium occupying the spaces between the tetrahedrons and surrounded by halides with coordination numbers of 8 or 9, depending on the Cs site (as shown in **Figure 1**b and Figure S2d, Supporting Information). The Zn-Cl tetrahedrons display anisotropy in their bond length,[12] resulting in asymmetrical tetrahedrons with geometrical deviations from standard tetrahedrons due to unequal electrostatic forces and charges inside the unit cell. The powder X-ray diffraction (pXRD) spectrum confirms the expected orthorhombic phase for Cs_2ZnCl_4 and Cs_2ZnBr_4 compositions, as shown in Figures S1b and S2b (Supporting Information), respectively.

The optical measurements (Figure S1a, Supporting Information) of the Cs_2ZnCl_4 NPs reveal an absorbance spectrum with an onset at a wavelength of 295 nm and a photoluminescence (PL) maximum peak at a wavelength of 380 nm, with a long tail that ends at 550 nm in agreement with previous reports.[17] Similar optical features were observed for Cs_2ZnBr_4, as indicated in Figure S2a (Supporting Information). These NPs have the potential to function as a scintillator[9,18] due to their wide range of absorbance from deep UV to X-ray region and their emission in the UV–vis range. Previous reports suggest that the low PLQY (12.5% for Cs_2ZnCl_4 and ≈11.5% for Cs_2ZnBr_4, Figure S16a, Supporting Information) may be related to a fast component of non-radiative auger free luminescence[10,11] that can be observed in Cs_2ZnX_4 compositions. Moreover, the self-trapping exciton mechanism can explain the anomaly in the PL signal that appears as a long tail, due to the existence of different energy traps at the band gap.[20]

The synthesis parameters to produce Cs_2ZnX_4 nanoparticles (NPs), such as temperature and growth time, were precisely tuned to obtain NPs with different sizes and shapes (inset of Figures 2a and 3c,d). Figure 1a displays a high-angle annular dark-field scanning transmission electron microscopy (HAADF-STEM) image of Cs_2ZnCl_4 NPs that were synthesized at a temperature of 150 °C with a growth time of 30 s (growth time corresponds to the time from the injection of the precursor until quenching by an ice bath). In Figure S2c (Supporting Information), Cs_2ZnBr_4 NPs were synthesized at a temperature of 125 °C with a growth time of 30 s. These parameters were carefully selected to achieve a variety of distinct morphologies for the NPs.

Under certain temperature and growth conditions, Cs_2ZnX_4 NPs can exhibit two different shapes, either rod-like or polygonal, depending on their position. The self-assembly of the NPs is driven by the interactions between the ligands, as illustrated in Figure S4a (Supporting Information). The rod-like shape is typically observed for NPs that are assembled with a constant spacing of 2.6 ± 0.3 nm between them (Figure S5a–c, Supporting Information), while the polygonal shape is observed for unassembled NPs that lie flat on their face. These two perspectives represent the same NPs viewed from different orientations, as confirmed by EDS analysis (Figure S1c–f, Supporting Information) and FFT (Figure S1g,h, Supporting Information). Additionally, plasma treatment was utilized to eliminate the ligand interactions (Figure S3a–f, Supporting Information) and switch between the two shapes.

The HR-TEM analysis presented in Figure 1g,h and Figure S12 (Supporting Information) (Figure S11, Supporting Information for Cs_2ZnBr_4) revealed that the damaged areas within the nanoparticles were not entirely hollow from one side of the particle to the other. Instead, there is a damaged area in the inner part of the particle that is trapped within a thin crystalline layer that remains as a shell above and below the area. The HR-TEM images in Figure 1g,h showed clear lattice images in the zone axis of both the damaged and undamaged regions of the particles. The FFT of the damaged area (inset of Figure 1g) demonstrated an electron diffraction pattern with a d-spacing value of 0.150 corresponding to the crystallographic plane (281) of the orthorhombic phase. The lattice image in the undamaged area is shown in Figure 1h, with the FFT inset of Figure 3f corresponding to the crystallographic plane (513) of the same orthorhombic phase as the damaged area. This indicates that the remaining thin crystalline layer in the damaged area has preserved the original structure of the particle.

To confirm the presence of a thin layer in the damaged areas, an inverse FFT (IFFT) simulation was performed on the bottom right inset of **Figure 2**e, which demonstrated a defined lattice pattern that matched the IFFT simulation of the original complete area (bottom right inset of Figure 2f). Additionally, the e-beam (counts) intensity analysis over time (Figure S8, Supporting Information) of a specific area showed a increase in intensity followed by a subsequent decrease back to the original intensity values prior to the damage, indicating in situ self-healing.

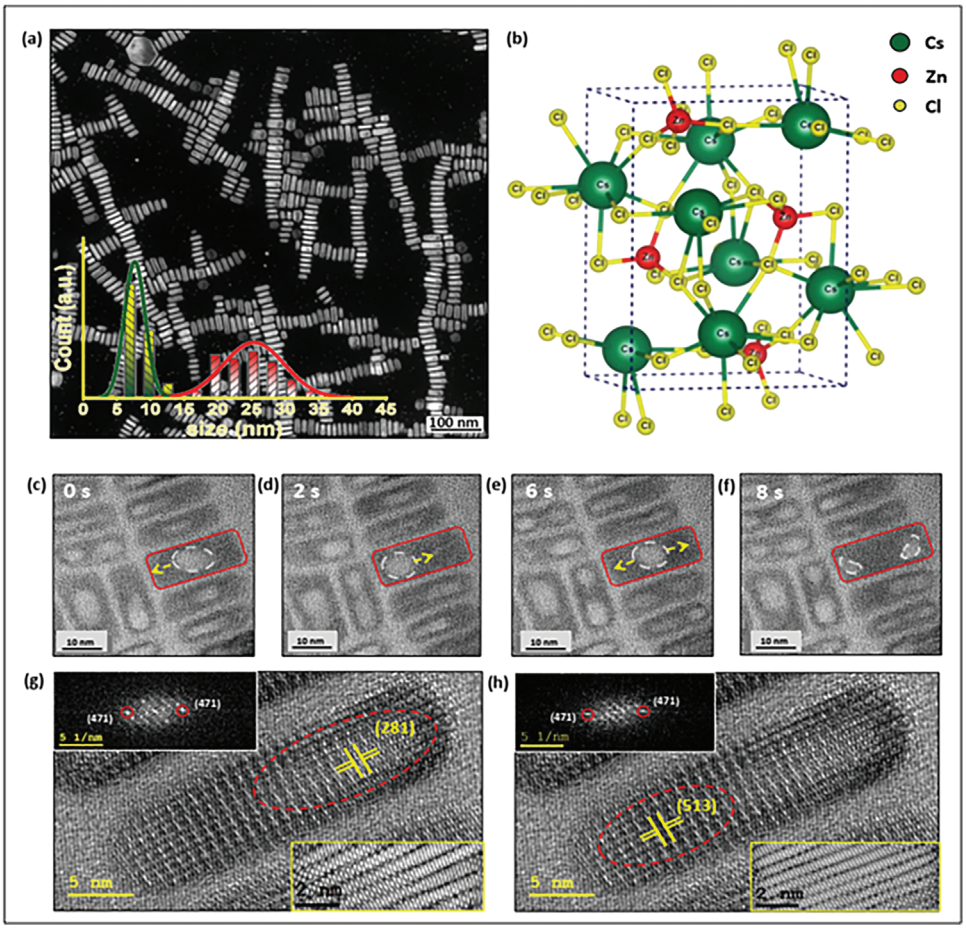

Figure 1. Dynamic self-healing behavior of Cs_2ZnX_4 NPs. a) A high-resolution transmission electron microscopy (HR-TEM) image shows the resulting self-assembled NPs, which exhibit a size distribution of 34.5 ± 4.3 nm in length (red) and 7.9 ± 1.7 nm in width (green). b) The unit cell[19] of the Cs_2ZnCl_4 crystal structure. c–f) A series of HR-TEM images, indicating the self-healing ability of the NPs. The white area, marked by a dashed white line, represents the damaged region prior to healing. The images show the dynamic movement of the damaged area within the frame of the NPs over time. g,h) Fast Fourier transform (FFT) analysis of a single NP, revealing the crystallographic planes (281) in the damaged (white) area and (513) in the undamaged (dark) area as well as (471) plane in the FFTs' left inset analysis, both belonging to the expected orthorhombic phase. The inset in the bottom right corner of panels (g,h) presents an inverse FFT simulation of the remaining lattice in the damaged area with an original expected structure.

Furthermore, after the healing process, the healed part of the nanoparticle was reconstructed back to its original phase and structure, a conclusion supported by live FFT analysis as shown in Figure S6 and Movie S4 (Supporting Information). The FFT results (Figure S6a–c, Supporting Information) showed the same crystallographic planes of (193) and (510) with d-spacings of 0.124 and 0.938 nm, respectively, before and after the healing process.

Based on the previous observations, we utilized electron beam radiation to create temporary nanoshells (NSs) from the nanoparticles . By employing a high acceleration beam voltage (300 kV) and a current density of 2.5–6.5($\times 10^4$) e A^{-2}, the formation of NSs from the as-synthesized NPs was achieved. The HAADF intensity line scan confirmed a significant decrease in intensity at the inner part of the NSs (Figure S10a–d, Supporting Information).

The Cs_2ZnCl_4 NSs are displayed in the dark-field STEM image in Figure 2a (Cs_2ZnBr_4 NSs can be observed in Figure 4a). The NSs exhibited a polygonal morphology, with some of them appearing in a rod-like shape. In contrast, **Figure 3**a displayed NSs that were synthesized with a short growth time and had a good size distribution, which enables the self-assembling process.

An EDS line scan was carried out on the polygonal shell (Figure 2e) to determine the chemical composition of both the shell and the thin layer remaining in the inner part of the NPs. The inset in Figure 2e shows the direction of the EDS line scan. The scan revealed a clear reduction in the elements present in the NPs' inner part. This was further supported by a high-resolution EDS scan also of Cs_2ZnBr_4 (Figures S13a–f and S14a,b, Supporting Information). Despite the significant decrease in the material signal in the inner part of the NSs, the element signals did not drop to zero, indicating the presence of a remaining crystalline thin layer that was also observed during dynamic self-healing. A lattice image of the inner part of the NSs with corresponding FFT for Cs_2ZnCl_4 (Figure S12a,b, Supporting Information) and for Cs_2ZnBr_4 (Figure S11a–c, Supporting Information) was obtained. A similar observation was made by the EDS line scan in the case of the rod-like shape, as shown in Figure 2f (and Figure S9a–c, Supporting Information).

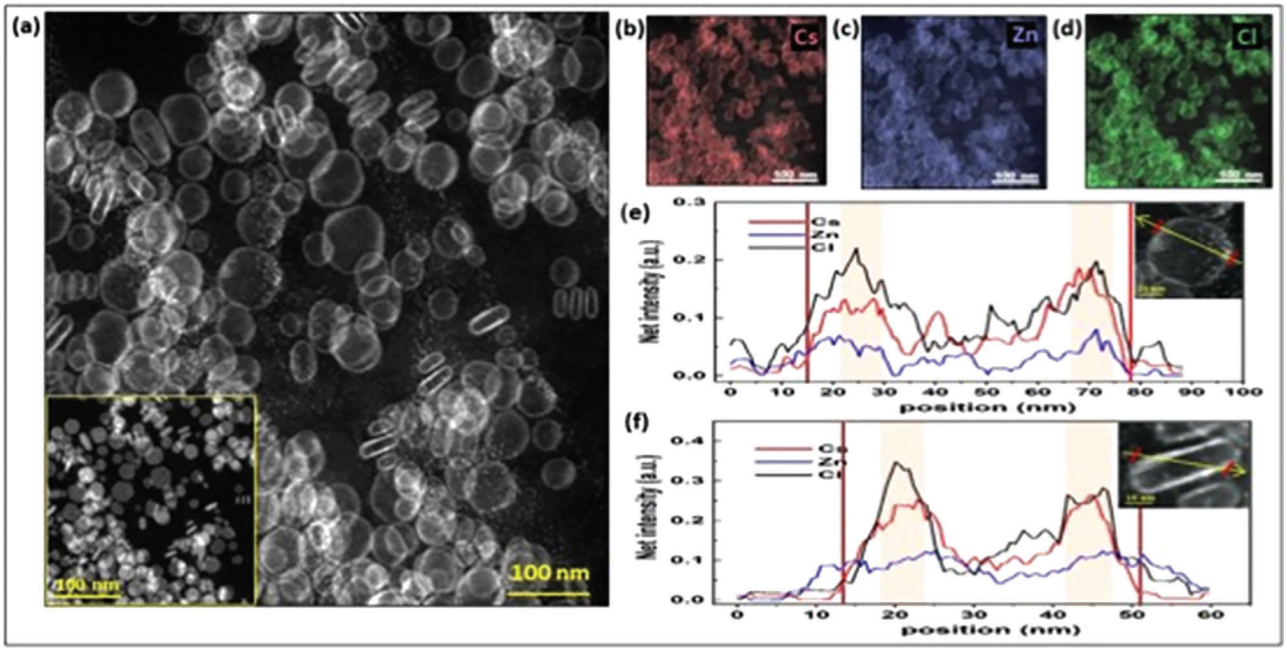

Figure 2. Cs_2ZnCl_4 nanoshells formed by the electron beam radiation of the HR-TEM. a) HAADF-STEM image of the obtained nanoshells after the electron beam radiation. The inset shows the NPs before the electron beam radiation. b–d) EDS elemental analysis distribution of the NSs. e,f) EDS line scan of single NSs indicating the increase of Cl and Cs at the shell of the NP, and the significant decrease of the elements in the inner damaged area of the NP. The red lines on the graph indicate the start and end points of the scan. Both scans show the existence of a thin layer that remains at the bottom of the NSs. In the case of polygonal morphology (e), and in the case of rod-like morphology (f).

In Figure 3, we present the NPs obtained under different initial conditions along with their corresponding NSs. Specifically, Figure 3c illustrates the NPs synthesized at 150 °C and with a growth time of 30 s, while Figure 3d shows NPs synthesized at 120 °C and with a growth time of 180 s, exhibiting a rectangular morphology. The resulting NSs can be observed in Figure 3a,b, respectively. Clearly, the shape of the NSs closely resembles the original morphology of the as-synthesized NPs, suggesting a high degree of shape preservation during the conversion process.

The inherent self-healing ability of the NPs enabled the complete healing of the NSs back to their original NPs. The Cs_2ZnBr_4 NSs, as shown in **Figure 4**a,b, and the Cs_2ZnCl_4 NSs, as illustrated in Figure 4f–h, underwent a wide range of self-healing and reverted back from their shell state to the as-synthesized NPs. An

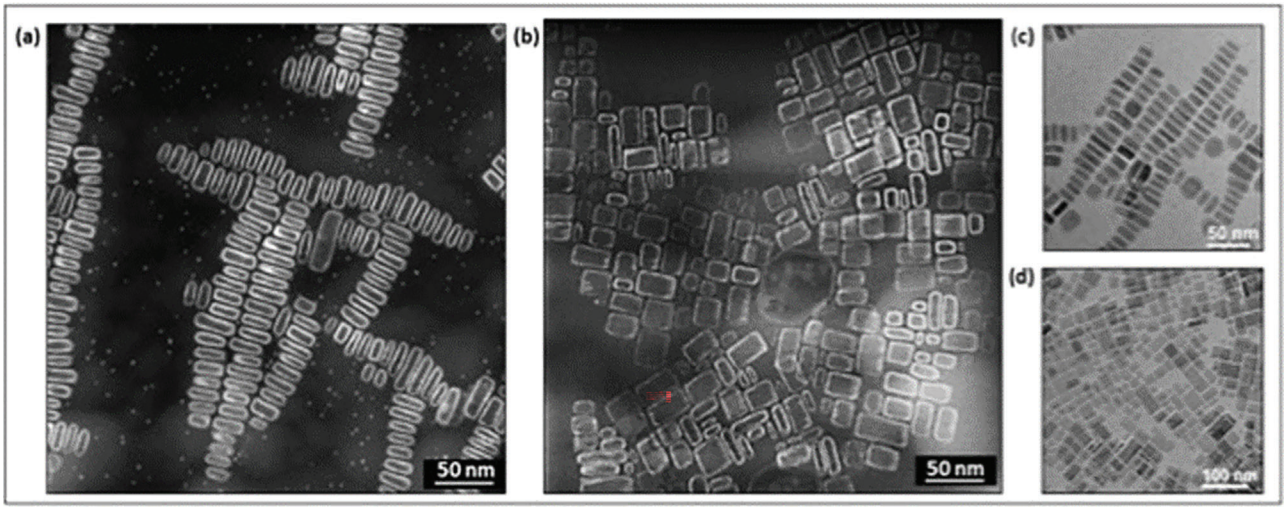

Figure 3. Cs_2ZnCl_4 NSs at different temperatures and growth times fabricated by electron beam radiation. a) HAADF-STEM image of the resulting NSs synthesized at a temperature of 150 °C and 30 s growth time b) HAADF-STEM image of 120 °C and 180 s growth time—rod-like morphology. c) HR-TEM images of the NSs presented in (a) before the electron beam radiation and d) HR-TEM images of the NSs presented in (b) before the electron beam radiation.

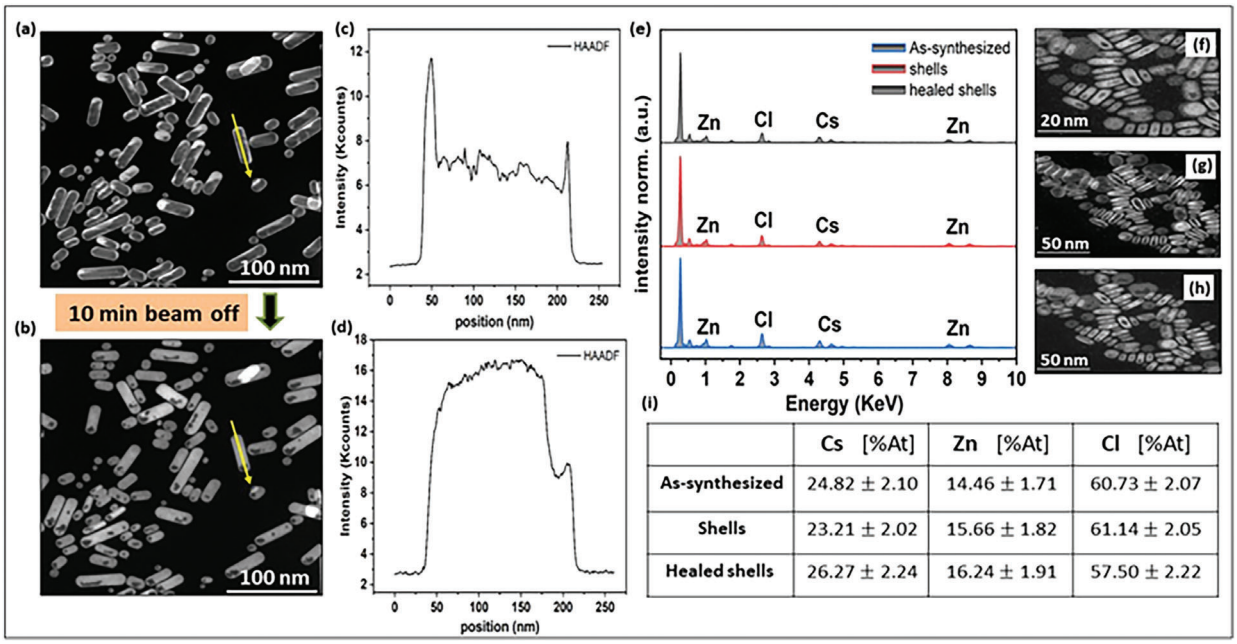

	Cs [%At]	Zn [%At]	Cl [%At]
As-synthesized	24.82 ± 2.10	14.46 ± 1.71	60.73 ± 2.07
Shells	23.21 ± 2.02	15.66 ± 1.82	61.14 ± 2.05
Healed shells	26.27 ± 2.24	16.24 ± 1.91	57.50 ± 2.22

Figure 4. Healing from shells state back to complete NPs. a) HAADF-STEM image of Cs_2ZnBr_4 nanoshells, and the shells' healing after blocking the e-beam for 10 min. b,c) HAADF intensity line scan profile of the marked shell in (a), indicating the strong intensity decrease at the inner part compared with the outer frame. d) HAADF intensity line scan profile of the same marked shell in an after the healing marked in (b), indicating the HAADF increased intensity after the healing to the undamaged frame values shown in (c). e) EDS analysis of three states of Cs_2ZnCl_4 NPs indicates the same elemental composition for all three states in the same field of view and scanning parameters, and i) as indicated by the elemental ratio. f–h) HAADF-STEM images of the same field of view analyzed by the EDS in (e), as-synthesized NPs state (f). The nanoshells state (g). The healed shells state (h).

additional HAADF intensity line scan was performed to further support the healing process of the material from the NSs stage to the complete NPs. The HAADF line scan showed a strong signal decrease for the inner part of the NP in the shell stage, as shown in Figure 4c, which corresponded to the arrow in Figure 4a. In contrast, the signal increased after the healing process, as shown in Figure 4d, corresponding to the arrow in Figure 4b. Moreover, Figure 4e,i presents the (EDS) analysis for the three different stages of the NPs: the as-synthesized stage, the shell stage, and the healed shells (Figure 4f–h, respectively), indicating the same elements and composition ratio (Figure 4i) in all stages. This confirms that the original phase and structure of the NPs were preserved during the various healing processes. The EDS analysis also supported the requirement that the material must remain inside the NPs during the shell reconstruction process in order to be able to self-heal back to the complete as-synthesized NPs. **Figure 5**a–c presents a schematic illustration of the various stages of shell healing under the electron beam, along with their corresponding STEM images.

Figure 6g shows the unnormalized counts of the EDS analysis of the same field of view (Figure 6h,i) and scanning parameters for the as-synthesized stage compare with the healed shells stage. It can be observed from the EDS counts (Figure 6g) that all of the elements have the same counts in the healed shells stage compare with the as-synthesized stage with a minority increase in the case of the Zn element.

A series of HAADF-STEM selected images captured at different time intervals under the same conditions are presented in Figure 6a–e, while the full movie can be found in Movie S5 (Supporting Information). At $T = 17$s (Figure 6b), the particle incurred visible damage, which was confirmed by the decrease in HAADF signal intensity shown in Figure 6f at the corresponding time. However, this damage was fully healed at 18 s (Figure 6c), in agreement with the HAADF signal as depicted in Figure 6f. Subsequently, similar damage occurred at 29 s and was healed at 34 s (Figure 6d,e), again in agreement with the HAADF signal shown in Figure 6f. A live HAADF signal analysis of the healing process is shown in Movie S6 (Supporting Information) indicating the various damage and healing processes in agreement with the HAADF signal. The reported NPs exhibited excellent stability for over 30 days of measurement under ambient conditions, as indicated in Figure S16b (Supporting Information) and by the powder X-ray diffraction (XRD) analysis in Figure S16c,d (Supporting Information). HR-TEM images of the NPs after 30 days at ambient conditions, presented in Figure S17a–c (Supporting Information), indicated no change in morphology. Furthermore, the PLQY of the NPs was measured for over a month (Figure S16a, Supporting Information), with an average PLQY of $12.5 \pm 1.0\%$ and $9.4 \pm 1.0\%$ for Cs_2ZnCl_4 and Cs_2ZnBr_4, respectively, demonstrating the stability of their optical properties. The self-healing ability, along with the proven structural and optical stability, makes these NPs a promising candidate for self-healing scintillators in the field of optoelectronic applications.

3. Discussion

The heating of specimens due to inelastic scattering of e-beams during transmission electron microscopy analysis is a widely acknowledged phenomenon, which has been previously reported.[21–23] For instance, the electron beam was observed to

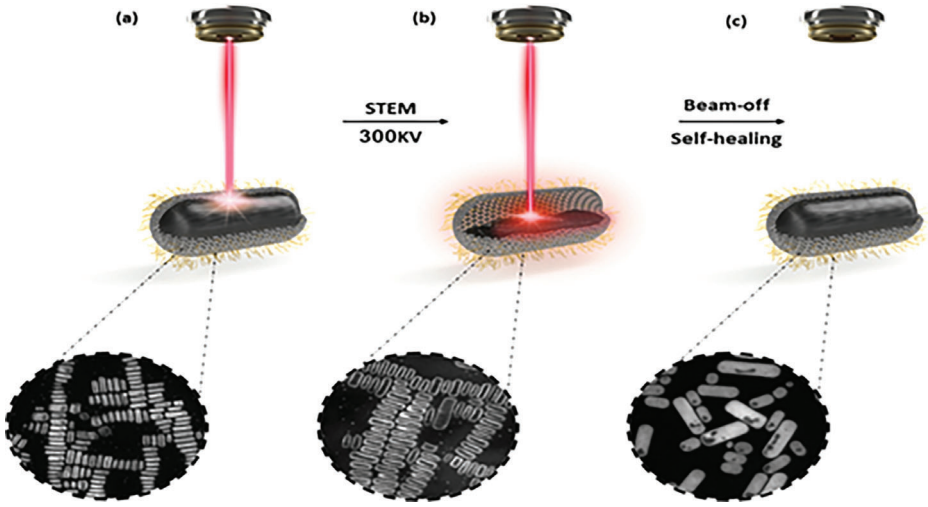

Figure 5. Schematic illustration of NSs formation and healing. a) As-synthesized NPs before the formation of the shells. b) NSs formation and original morphology preservation under 300 kV e-beam irradiation in STEM mode. c) Self-healed NSs back to the as-synthesized NPs by turning off the e-beam for 10 min.

cause the melting of bismuth nanoparticles at 180 °C,[24,25] heating up to 200 °C of Al-Si alloy particles,[26] and a temperature increase of up to 300 °C in $LiTiO_3$.[27] The extent of local heating resulting from e-beam exposure is influenced by various factors, including the current density,[21] electron energy[27] (acceleration voltage), and the material's thermal conductivity.[26] Even high thermal conductive materials ($\kappa > 100$ WK^{-1} m^{-1}) can generate substantial heat at high current doses induced by electron-beam exposure.[22] At high acceleration voltages, such as those utilized in this study, the radiolysis effect can be neglected since the majority of the electrons pass through it. According to Lindemann's criterion Melting is considered to be a first-order phase transition, which occurs when the amplitude of the thermal vibrations of the atoms and their resulting displacements reach a critical value that is a fraction of the lattice constant. In such cases, the material ceases to be an immobilized solid and becomes molten or quasi-molten,[27,28] even at temperatures below its melting point, resulting in atoms' high mobility.[29]

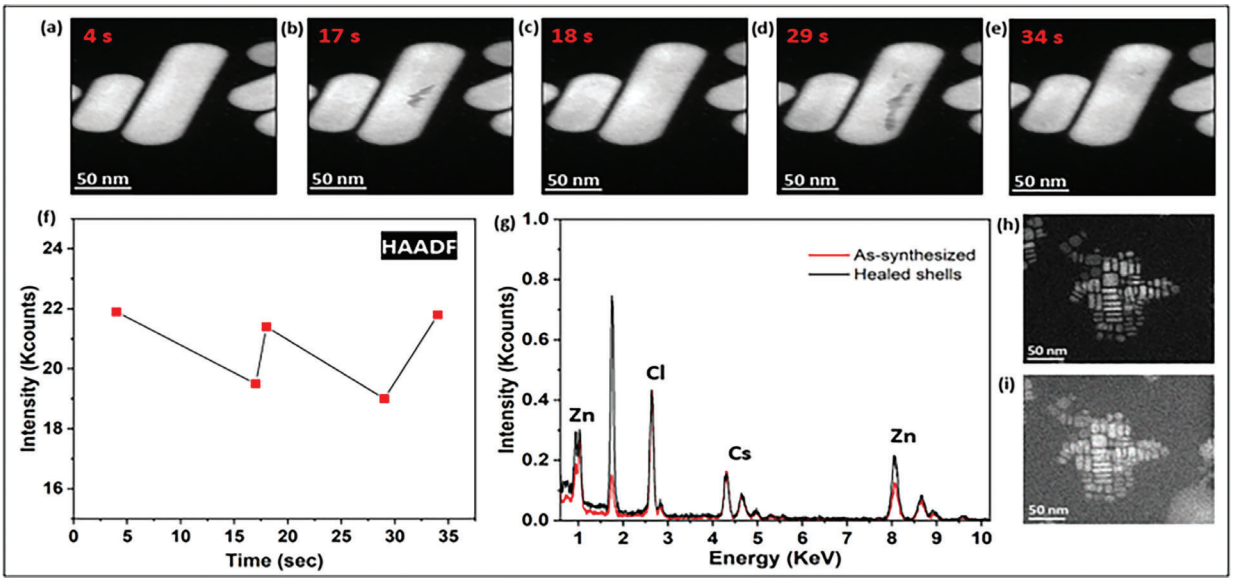

Figure 6. Full self-healing of the presented NPs. HAADF-STEM images of the NPs in a different times. a) The NPs before the damage. b) The first created damage at $T = 17$s appearing as small gray area, and c) the self-healing and disappearance of the damage at time $T = 18$ s. d) Another created damage at time $T = 29$ s, and e) the damage healing at time $T = 34$s. f) HAADF intensity profile analysis in a time of the corresponding NPs in (a–e) at the damaged and healed area, indicating the intensity decrease at the times at which damages are appearing ($T = 17$, 29 s) and the increase back to the original values after the healing ($T = 18$, 34 s) as before the first damage ($T = 4$ s). g) Quantitative EDS analysis by counts of the h) two different as-synthesized and i) healed shells states, indicating the same intensity counts for the absolute majority of the presented elements. (The extra pick at 1.75 keV belongs to Si and not affecting the relevant elements counts).

During the electron beam irradiation process, we utilized a field emission gun to generate an electron beam with a small beam diameter and a high current density of up to 6.5 ($\times 10^4$) e A^{-2}. This high current density can cause significant local thermal vibrations and heating of the sample, as demonstrated in previous studies.[22,30] To estimate the melting temperature of the nanoparticles (NPs), we conducted a differential scanning calorimetry (DSC) measurement, which showed an initial melting onset at a temperature of 293.3 ± 3 °C, as shown in Figure S15 (Supporting Information). Moreover, since the HR-TEM imaging was performed under ultra-high vacuum conditions inside the TEM column (5.9–8.8 ($\times 10^{-8}$) Torr), and with high current doses, significant local heating is likely to be generated under the e-beam, resulting in atomic displacement[22] and diffusion[27] in the NPs which is observable in Figure 1c–f and Movies S1–S3 (Supporting Information). The electron beam signal analysis (Figures S7 and S8, Supporting Information) and HAADF imaging (Figure S10, Supporting Information and Figure 4c,d) confirm that the density of the material was altered due to the e-beam radiation at the inner part of the NPs and the NSs. Based on the EDS counts in Figure 6g, it can be concluded that the absolute majority of the material remains inside the NSs, and therefore, we can exclude image contrast variation due to a lower amount of material. The local heating generated by the e-beam causes vibrations and atomic displacements, which lead to a local decrease in the density of the material and changes in inter-atomic distances, as observed in the NSs shown in Figures 2a and 3a,b and for the dynamic healing (Figure 1c–f), resulting in image contrast deviation.

High-resolution lattice images (Figure 1g,h for the dynamic damage and Figures S11a and S12a, Supporting Information for the shells state) and EDS analysis (Figure 2e,f) confirmed the presence of a thin crystalline layer that remains as a shell around the particles in all forms of damage. The remaining layer is protected from damage by the organic ligands that hold it (Figure 5a–c). These ligands consist of atoms with a low atomic number (<9) that are transparent to the beam at high acceleration voltages. Most of the beam's impact and interactions with the sample occur in the inner region of the particle, where heavy atoms are located at a higher density. The structure of the unit cell features halides (Cl/Br) that protrude out (Figure 1b and Figure S2d, Supporting Information for Cl, Br respectively) and carry a partial negative charge. This creates a platform for ion–dipole interactions with the positively charged oleyl amine ligand, resulting in strong ion–dipole interactions between the ligands and the particles (Figure S4b, Supporting Information). These interactions are strong enough to create a shell that is protected from beam damage and remains as a highly crystalline shell around the particle.

Furthermore, the NPs can heal themselves back from the shell state to the complete full particle since all the primary amount of the damaged material remains inside the particle. The remaining crystalline shell serves as a protective barrier, preventing the material from escaping during the damage and healing phases until the particle has completely healed itself. After the healing process, the particles return to their original crystallographic structure, as confirmed by quantitative EDS analysis (Figure 6g). In some cases, the same crystalline shell can be utilized as a guiding template[28] in the self-healing process to obtain the original crystallographic structure. A similar effect of ligands as protection in creating damage by the beam and self-healing initiation has been recently reported for double perovskite.[8]

To deepen our understanding of the dynamic self-healing processes and the formation of damage, we conducted a detailed study under various irradiation conditions. Three different acceleration voltages (80, 200, and 300 kV) were measured at three different doses (50, 200, and 500 e A^{-1} s^{-1}). Our findings indicate, that for a given acceleration voltage and dose, the size of the damage linearly increases with irradiation time (Figure S18a–f, Supporting Information). Additionally, for a given acceleration voltage, the damage growth rate increases with the defined dose (Figure S19a–c, Supporting Information). Based on that it is possible to extract the damage growth rate (Figure S20a–c, Supporting Information) for each initial dose at a given acceleration voltage. Our results indicate that the growth rate increases with the defined starting dose and that the size of the damage linearly increases as a function of the irradiation time under constant irradiation conditions. Moreover, by monitoring the temporal evolution of initial damage formation and subsequent healing processes under different irradiation conditions, it is possible to establish an inverse relationship between the time required to initiate damage, the healing process and the magnitude of the defined dose for a given acceleration voltage (Figure S21, Supporting Information). At a fixed acceleration voltage, an increased dose results in a higher number of electrons reaching the sample over a given time, leading to an accelerated rate of damage growth in agreement with previous reports.[26,31] In contrast, higher acceleration voltages lead to large number of electrons passing through the sample,[22,30] resulting in fewer electron–sample interactions and a slower rate of heat generation. Therefore, it is necessary to employ longer irradiation times when using higher acceleration voltages to induce damage and observe subsequent healing.

In addition, by maintaining a constant dose of 2000 e A^{-2} s^{-1} and utilizing a fast integration time of 10 ms, we were able to record fast videos at three different acceleration voltages, from which we extracted dynamic self-healing velocity data. The obtained values of 25.8, 10.8, and 7.6 nm s^{-1} for acceleration voltages of 80, 200, and 300 kV, respectively, indicate an inverse relationship (Figure S22, Supporting Information) between acceleration voltage magnitude and the self-healing velocity. This trend may be attributed to additional processes that become dominant at higher acceleration voltages, such as sputtering and knock-on processes that can slow the dynamics of the healing process.[30]

To support our hypothesis that the damage in our samples was caused by local heating from the electron beam, we conducted an experiment using an in situ heating stage that enabled us to heat the sample during TEM measurements. We set a constant minimum dose (<25 e A^{-2} s^{-1}) and a moderate acceleration voltage of 200 kV to minimize the effect of the electron beam. The resulting damage observed at all temperatures was identical to that caused by the electron beam, and similar self-healing processes were initiated. This suggests that the electron beam is locally heating the sample which creates the damage. Therefore, the local heating generated by the beam and by direct heating is the same. Figure S23b (Supporting Information) shows a linear relationship between the size of the damage and the temperature similar to obtained linear relation between damage size and dose/irradiation time (Figure S18d–f, Supporting

Information), which allowed us to extract a damage growth value of 0.021 nm $°C^{-1}$. This value is approximately the same (95.5%) as the damage growth rate obtained for an irradiation dose of 50 e A^{-2} s^{-1} at an acceleration voltage of 80 kV (Figure S20a, Supporting Information). Additionally, we noted a direct relationship between the temperature and the increase in the damaged area (which is approximately the shape of a circle). The damage area values ranged from 25.0–77.3 nm^2 for the temperature range of 50–250 °C (Figure S23a, Supporting Information).

An additional important point for the discussion is related to the mode of transmission electron microscopy. In the case of using transmission mode (TEM), where the e-beam is located on the particles in a parallel point-like manner perpendicular to the specimen, the resulting damage is localized. This leads to a dynamic self-healing process, where the damaged areas move within the particle and continuously heal. On the other hand, when using scanning transmission electron microscopy (STEM), which employs a fast scan and a penetrating convergent beam[32,33] that is aligned at an oblique angle to sample with higher acceleration voltage (300 kV) and dose, the resulting damage is uniform and homogeneous, affecting the entire interior of the particle, resulting in the formation of shells. The accurate interpretation of electron microscopy images is contingent upon the exclusion of potential artifacts that can impact our diagnosis. One major artifact is astigmatism, which can cause blurring or distortion of the image resulting from an incorrect focusing of the electron beam in the focal plane.[32–34] By carefully performing alignment of the beam, astigmatism can be avoided. Other forms of aberrations, such as chromatic and spherical aberrations resulting from an incoherent beam, mostly affect image resolution and do not create artifacts. The charging effect, which results from the accumulation of charges on the sample, can be mitigated by using high acceleration voltage TEM,[32] and due to the semi-conducting nature of the sample, the buildup of charge is negligible. Additionally, aberration correctors are commonly employed in high-voltage microscopes (especially in Themis Z we utilized) to minimize artifacts and enhance resolution. In our study, we used three different electron microscopes, fine-tuning the alignments to minimize artifacts and carefully preparing the samples to prevent artifacts resulting from impurities and carbon. Additionally, we conducted an experiment to minimize the intensity of the electron beam in terms of dose and heated the sample in situ to isolate the effects of heating, observing the same phenomena as under the electron beam.[33] (Comprehensive explanation and discussion of potential artifacts in TEM and STEM, as well as required alignments and strategies to avoid them, can be found in the Supporting Information).

4. Conclusions

In this work, we presented the self-healing process of non-toxic metal halide nanoparticles. Specifically, we demonstrate the in situ dynamic self-healing as well as extensive shells healing of two compositions of Cs_2ZnX_4 (X = Cl, Br) NPs created by electron beam radiation, and use nanoscale advanced methods to elucidate the self-healing mechanism. We found that despite extensive atomic displacement and diffusion resulting from local heating caused by the electron beam, the original morphology, composition, and quantity of the NPs remain completely identical after the self-healing process. We established connections between the healing velocity and damage size as a function of the dose and defined acceleration voltage. Our in situ measurement during sample heating, while minimizing the effect of the beam, confirmed that the heat generated by the beam plays a role in the damage and in the healing processes. The self-healing process is facilitated by a thin crystalline layer that remains around the NPs following e-beam radiation, which functions as a template for self-healing and prevents the damaged material from escaping. The self-healing ability of these low-toxicity NPs offers a promising route to developing self-healing scintillators and optoelectronic components that require atomic-level damage healing abilities and long-term stability.

5. Experimental Section

Materials: Zinc (ii) acetate ($Zn(Ac)_2$, ≥ 99.99%, Sigma-Aldrich), cesium (i) acetate (CsAc, ≥ 99.99%, Sigma-Aldrich), benzoyl chloride (Bz-Cl, 99%, Sigma-Aldrich), benzoyl bromide (Bz-Br, 97%, Acros Organics) oleic acid (OA, 90%, Sigma-Aldrich), oleyl amine (OAm, 70%, Sigma-Aldrich), 1-octadecene (ODE, 90%, Alfa Aesar), *n*-hexane (HPLC grade, 95%, Sigma-Aldrich) all materials were used as received without any further purifications.

Preparation of Cs_2ZnX_4 NPs: In a typical synthesis[17] 0.4 mmol of $Zn(Ac)_2$ and 0.2 mmol of CsAc were loaded into 100 mL 3-neck flask with addition of 1 mL OA and 1 mL OAm all dispersed in 2 mL ODE. The solution was degassed and dried for 1 h under vacuum at 120 °C and then heated in order to be injected at temperature of 90–180 °C under Argon gas, based on the hot-injection method. Next, The NPs formation was carried out by injecting 200 µL of Bz-Cl (220 µL of Bz-Br for Cs_2ZnBr_4 preparation) dispersed in 0.5 mL ODE to the reaction mixture. The reaction was quenched after 30–180 s using an ice bath. The crude solution was then centrifuged at 4000 rpm for 5 min and the resulting precipitation was redispersed in hexane for further characterization.

Plasma Treatment: The treatment was carried out by deposition of the NPs on a glass substate. Next, the glass substrates with the NPs were treated by plasma (80% power, diener electronics Atto, 100 W) under oxygen flow for 0–15 min.

Optical Measurements: The absorbance spectra were taken by using a Jasco V-670 spectrophotometer, and the photoluminescence (PL) spectra were measured by a HORIBA scientific FluoroMax-4 fluorometer with 150 W CW ozone free xenon arc lamp using excitation wave length of 290 nm fixed by monochromator. The PL signal was detected by photon counting detector (R928P photomultiplier tube) and a reference UV-enhanced silicon photodiode. Photo luminescence quantum yield (PLQY) was measured using Hamamatsu absolute PLQY spectrometer C11347 and excitation wavelength of 380 nm fixed by a monochromator. In all of the optical measurements, the NPS were dispersed in hexane measured in a quartz cuvette.

Powder X-Ray Diffraction (XRD): X-ray powder diffraction measurements were performed by D8 advance diffractometer (Bruker AXS, Karlsruhe, Germany) with secondary graphite monochromator, 2° Soller slits and 0.2 mm receiving slit. XRD patterns within the range of 3–60° 2θ were recorded at room temperature using CuKα radiation (λ = 1.5418 Å) with the following measurement conditions: tube voltage of 40 kV, tube current of 40 mA, step scan mode with step size of 0.02° 2θ, and counting time of 1–3 s per step. The samples were placed on low background quartz holder.

High Resolution Transmission Electron Microscopy (HR-TEM): Morphology and structure were analyzed by HR-TEM Tecani F20 G2 (FEI company, USA) operated at 200 kV acceleration voltage. Sample preparation was performed as follow: 2.9 µL of the NPs dispersion were dropped on ultrathin copper grid coated with an amorphous carbon layer (400 mesh). Next, the grid was placed in a vacuum chamber for solvent evaporation and then slightly heated to 50 °C to minimize carbon contamination. The

dynamic self-healing was observed under current density range of 1.2–2 ($\times 10^4$) e^- A^2 with spot size one and an objective aperture of 400 µm in a bright field mode. In order to observe the nanoshells, a current density range of 2.5–6.5 ($\times 10^4$) e^- A^2 under 300 kV in a dark field (HAADF-STEM) mode were performed. The various irradiation conditions of the dynamic self-healing experiment were carried out in TEM mode using a Themis Z type microscope with aberration correction. The acceleration voltage was varied between 80 and 300 kV, while the dose ranged from 50–500 e A^{-2} s^{-1}. The captured videos were recorded in 4 K resolution with a frame integration and time interval of 1 s. A 10 um aperture objective was utilized in all the recorded videos. The self-healing speed was determined for each acceleration voltage at a constant dose of 2000 e A^{-2} s^{-1}, with a prime integration and time interval of 40 ms.

In Situ Heating Measurement: Was performed by an in situ heating double tilt heating holder Gatan 652. The measurement was carried out in TEM mode by Themis Z aberration corrector microscope (Thermo Fisher Scientific) operated at 200 kV under dose <25 e A^{-2} s^{-1}. Integration time determined to 0.25–1000 s at a resolution of 1024*1024 px.

Energy Dispersive X-Ray Spectroscopy (EDX): Elemental analysis and composition were performed by high angle annular dark filed (HAADF) scanning TEM (STEM) Themis Z (Thermo Fisher Scientific) operated at 80–300 kV accelerating voltage. The X-ray emission was detected by super-X EDS detector. Sample preparation was similar as in HR-TEM analysis. The current density used to fabricate the NSs were in the range of 2.5–6.5 ($\times 10^4$) e^- $Å^{-2}$ under 300 kV acceleration voltage.

Differential Scanning Calorimetry (DSC): Melting points' onset was measured by STA Jupiter 449F3 (NETZSCH Geratebau GmbH), high-speed tungsten furnace and type S sensor with <1 uW resolution. The measurement was performed under N_2 environment and heating rate of 5 K min^{-1}.

Supporting Information

Supporting Information is available from the Wiley Online Library or from the author.

Acknowledgements

The authors would like to thank the Israel Science Foundation grant No. 937/18 and the Israel Ministry of Energy for the financial support during this project. A special thanks to Dr. Sergey Remennik for his continued support and scientific advice in the field of HR-TEM and STEM microscopy.

Conflict of Interest

The authors declare no conflict of interest.

Data Availability Statement

The data that support the findings of this study are available in the supplementary material of this article.

Keywords

low toxic, nanoparticles, self-healing

Received: July 9, 2023
Published online:

[1] M. Enke, D. Dohler, S. Bode, W. H. Binder, M. D. Hager, U. S. Schubert, in *Advances in Polymer Science*, Vol. *273*, Springer, New York LLC **2016**, pp. 59–112.
[2] M. Enke, D. Dohler, S. Bode, W. H. Binder, M. D. Hager, U. S. Schubert, in *Advances in Polymer Science*, Vol. *273*, Springer, New York LLC **2016**, pp. 113–142.
[3] M. Abdolah Zadeh, S. van der Zwaag, S. J. Garcia, in *Advances in Polymer Science*, Vol. *273*, Springer, New York LLC **2016**.
[4] N. Kuhl, S. Bode, M. D. Hager, U. S. Schubert, in *Advances in Polymer Science*, Vol. *273*, Springer, New York LLC, **2016**.
[5] S. Specht, J. Bluhm, J. Schröder, in *Advances in Polymer Science*, Vol. *273*, Springer, New York LLC **2016**.
[6] D. Chen, D. Wang, Y. Yang, Q. Huang, S. Zhu, Z. Zheng, *Adv. Energy Mater.* **2017**, *7*, 1700890.
[7] D. R. Ceratti, Y. Rakita, L. Cremonesi, R. Tenne, V. Kalchenko, M. Elbaum, D. Oron, M. A. C. Potenza, G. Hodes, D. Cahen, *Adv. Mater.* **2018**, *30*, 1706273.
[8] S. Khalfin, N. Veber, S. Dror, R. Shechter, S. Shaek, S. Levy, Y. Kauffmann, L. Klinger, E. Rabkin, Y. Bekenstein, *Adv. Funct. Mater.* **2021**, *32*, 2110421.
[9] K. Takahashi, M. Arai, M. Koshimizu, Y. Fujimoto, T. Yanagida, K. Asai, *Jpn. J. Appl. Phys.* **2020**, *59*, 072002.
[10] A. Ohnishi, M. Kitaura, T. Otomo, M. Sasaki, *J. Phys. Soc. Jpn.* **2003**, *72*, 2400.
[11] A. Ohnishi, M. Kitaura, M. Itoh, M. Sasaki, *J. Phys. Soc. Jpn.* **2012**, *81*, 114704.
[12] J. A. McGinnety, *Acta Crystallogr. 13*, 1058.
[13] X. Liu, C. Peng, L. Zhang, D. Guo, Y. Pan, *J. Mater. Chem. C* **2022**, *10*, 204.
[14] K. Sugawara, M. Koshimizu, T. Yanagida, Y. Fujimoto, R. Haruki, F. Nishikido, S. Kishimoto, K. Asai, *Opt. Mater.* **2015**, *41*, 53.
[15] P. J. Dereń, J. Derouet, P. Porcher, D. Svoronos, *J. Mol. Struct.* **1997**, *404*, 167.
[16] B. Su, M. Li, E. Song, Z. Xia, *Adv. Funct. Mater.* **2021**, *31*, 2105316.
[17] D. Zhu, M. L. Zaffalon, V. Pinchetti, R. Brescia, F. Moro, M. Fasoli, M. Fanciulli, A. Tang, I. Infante, L. De Trizio, S. Brovelli, L. Manna, *Chem. Mater.* **2020**, *32*, 5897.
[18] N. Hurley, F. Moretti, H. Yan, E. Bourret-Courchesne, Y. S. Chu, S. S. Wong, *J. Mater. Chem. C* **2020**, *8*, 8622.
[19] K. Momma, F. Izumi, *J. Appl. Crystallogr.* **2011**, *44*, 1272.
[20] O. D. I. Moseley, T. A. S. Doherty, R. Parmee, M. Anaya, S. D. Stranks, *J. Mater. Chem. C* **2021**, *9*, 11588.
[21] B. Fritsch, A. Hutzler, M. Wu, S. Khadivianazar, L. Vogl, M. P. M. Jank, M. März, E. Spiecker, *Nanoscale Adv.* **2021**, *3*, 2466.
[22] R. F. Egerton, P. Li, M. Malac, *Micron* **2004**, *35*, 399.
[23] H. Zheng, J. B. Rivest, T. A. Miller, B. Sadtler, A. Lindenberg, M. F. Toney, L.-W. Wang, C. Kisielowski, A. Paul Alivisatos, *Science* **2011**, *333*, 206.
[24] J. B. Wagner, M.-G. Willinger, J.-O. Müller, D. S. Su, R. Schlögl, *Small* **2006**, *2*, 230.
[25] Y. Li, et al., *Nat. Commun.* **2017**, *8*.
[26] T. Yokota, M. Murayama, J. M. Howe, *Phys. Rev. Lett.* **2003**, *91*, 265504.
[27] A. D. Romig, in Proceedings, Annual Conference – Microbeam Analysis Society, **1984**, pp. 7–13.
[28] T. Ben-David, Y. Lereah, G. Deutscher, J. M. Penisson, A. Bourret, R. Kofman, P. Cheyssac, *Phys. Rev. Lett.* **1997**, *78*, 2585.
[29] F. H. Macdougall, *J. Phys. Colloid Chem.* **1947**, *51*, 1032.
[30] R. F. Egerton, F. Wang, P. A. Crozier, *Microsc. Microanal.* **2006**, *12*, 65.
[31] H. Guo, P. Zhou, D. Natelson, J. Lou, *Microsc. Microanal.* **2017**, *23*, 1766.
[32] D. B. Williams, C. B. Carter, *Transmission Electron Microscopy*, Springer US, New York **1996**.
[33] D. J. Barber, *Opt. Acta* **1984**, *31*, 848.
[34] P. J. Goodhew, J. Humphreys, J. Humphreys, *Electron Microscopy and Analysis*, CRC Press, London **2000**.